Research article

Liuhao Zhu, Miaomiao Tang, Hehe Li, Yuping Tai and Xinzhong Li*

Optical vortex lattice: an exploitation of orbital angular momentum

https://doi.org/10.1515/nanoph-2021-0139
Received March 31, 2021; accepted May 25, 2021;
published online June 9, 2021

Abstract: Generally, an optical vortex lattice (OVL) is generated via the superposition of two specific vortex beams. Thus far, OVL has been successfully employed to trap atoms via the dark cores. The topological charge (TC) on each optical vortex (OV) in the lattice is only ±1. Consequently, the orbital angular momentum (OAM) on the lattice is ignored. To expand the potential applications, it is necessary to rediscover and exploit OAM. Here we propose a novel high-order OVL (HO-OVL) that combines the phase multiplication and the arbitrary mode-controllable techniques. TC on each OV in the lattice is up to 51, which generates sufficient OAM to manipulate microparticles. Thereafter, the entire lattice can be modulated to desirable arbitrary modes. Finally, yeast cells are trapped and rotated by the proposed HO-OVL. To the best of our knowledge, this is the first realization of the complex motion of microparticles via OVL. Thus, this work successfully exploits OAM on OVL, thereby revealing potential applications in particle manipulation and optical tweezers.

Keywords: micro-particle manipulation; optical vortex; orbital angular momentum; physical optics.

***Corresponding author: Xinzhong Li,** School of Physics and Engineering, Henan University of Science and Technology, Luoyang, 471023, China; and State Key Laboratory of Transient Optics and Photonics, Xi'an Institute of Optics and Precision Mechanics of CAS, Xi'an, 710119, China, E-mail: xzli@haust.edu.cn. https://orcid.org/0000-0002-6426-4043
Liuhao Zhu, School of Physics and Engineering, Henan University of Science and Technology, Luoyang, 471023, China; and State Key Laboratory of Transient Optics and Photonics, Xi'an Institute of Optics and Precision Mechanics of CAS, Xi'an, 710119, China
Miaomiao Tang and Hehe Li, School of Physics and Engineering, Henan University of Science and Technology, Luoyang, 471023, China
Yuping Tai, School of Chemical Engineering and Pharmaceutics, Henan University of Science and Technology, Luoyang, 471023, China

1 Introduction

In 1974, Ney and Berry discovered the dislocations in wave trains that inspired the interest in phase singularities and optical vortices [1]. In 1992, Allen et al. [2] discovered that photons possess orbital angular momentum (OAM), which afforded them an additional degree of freedom. An optical vortex (OV) possesses a helical phase, $\exp(jm\theta)$, and OAM, $m\hbar$, where m is the topological charge (TC) and θ is the azimuthal coordinate. OV exhibits many applications, including optical imaging [3], production of optical tweezers [4–7], and optical communication [8, 9]. To satisfy the requirements of versatile applications, an OV lattice (OVL) containing multiple unit OVs was extensively studied [10–19]. Generally, OVL is generated via the superposition of OV beams with the OV inlay in the intensity pattern.

As a typical OVL, in 2007, the optical Ferris light field was generated via the superposition of two Laguerre–Gaussian (LG) beams with specific pairs of TCs [20]. It could suitably trap cold and quantum degenerate atomic samples. In 2009, this beam was successfully applied to trap single rubidium (^{87}Rb) atoms [21]. In the same year, an ac-driven atomic quantum motor was proposed based on this beam [22]. To freely modulate OVL modes, a circular OVL was produced via the superposition of two concentric perfect optical vortices [23]. Furthermore, OVL was manipulated into versatile structures [24–26]. However, the dark core of OVL is barely exploited in atomic manipulation. It appears that the physical quantity of OAM on OVs in OVLs is being ignored. Why is this? The answer is concealed in the quantity of OAM. TC on a unit OV is always ±1, producing a negligible OAM of ±ħ per photon. Consequently, OAM, producing the "wrench force," in OVL has not been exploited. Conversely, the trapping and rotation of tiny objects are essential in some advanced applications, e.g., in light-driven motors [27, 28], detection of DNA rotation [29], hydromechanics [30], and cell sorting [31, 32].

Thus, OAM should be utilized, and OVL with high-order TC (HO-TC) should be developed. To address this challenge, in 2013, Chen et al. reported a kind of OVL with HO-OAM, which was generated via specific LG modes [33]. However, the number of OVs was related to their orders,

thus causing the unmodulation of the OVL mode. Further, in 2018, they modified the method to obtain arbitrary HO-OVL by employing several weighted factors [34]. Notably, a power index was applied to the complex amplitude of the LG beam in their methods, limiting the modulation of the mode for specific applications. These works motivated us to separate the complex amplitude of light into the amplitude and phase terms, which were modulated afterward.

Therefore, the major aim of this work is to develop a mode-controllable HO-OVL. In this paper, we first explained why TC of each OV in OVL is identically equal to ±1. Thereafter, following the definition of TC, the phase of the superposed optical field was separated and multiplied to obtain HO-TC. Moreover, by combining the arbitrary curve technique, the OVL structure was freely shaped, and the arbitrary HO-OVL was simultaneously obtained. Further, HO-TC of each OV was verified, and the energy flow and OAM around OV were analyzed. Finally, the physical quantity of OAM was exploited in OVL, after which experiments employing HO-OVL were performed to exhibit its application.

2 Principles and methods

To generate mode-controllable HO-OVL, two OV beams were shaped into desired arbitrary structures. Next, OVL was constructed via the superposition of these deformable OV beams. The complex amplitude of OVL was divided into the amplitude and phase terms. The phase term was extracted and modulated to obtain HO-TCs. Subsequently, the modulated phase multiplied the amplitude term to reconstruct a new complex amplitude of OVL, i.e., HO-OVL.

In addition, the generation of HO-TC of the unit OVs in OVL is crucial. Thus, the reason why OVs are always ±1 in OVL must be clarified. Let us begin from the definition of TC through the following [35]:

$$m = \frac{1}{2\pi}\int_C \nabla\psi(s)ds \tag{1}$$

where $\psi(s)$ denotes the OVL phase, C is a closed path around the singularity, i.e., the unit OV, and ∇ is the vector differential operator. Explicitly, the magnitude of TC depends only on the phase around the singularity.

The number of singularities on the circle can be deduced, as clarified in our previous work [23]. Here we attempt to answer the question, "why TC of unit OVs in OVL is always ±1?" For instances, Figure 1(a1) and (b1) shows the phase distributions of the two OV beams with TCs = –1 and 3, respectively. To facilitate the analysis, the phase ring was unrolled laterally into a rectangle and discretized to a sequence under the limiting conditions. The phase shown in Figure 1(a1) was discretized to an arithmetic sequence that started from a_q and possessed q terms [Figure 1(a2)], where $a_1 = 0$ and $a_q = 2\pi$. Similarly, the phase shown in Figure 1(b1) was discretized into three arithmetic sequences that started from b_1 and possessed p terms [Figure 1(b2)], where $b_1 = 0$ and $b_p = 2\pi$. Note that the size of each term was equal between Figure 1(a2) and (b2). In this case, $p = q/3$, i.e., the two OV beams were superposed completely, the interference petals appeared in absence of unit OVs [21, 23]. Then, let us consider that the two OV beams were partially superposed. Firstly, the phase shown in Figure 1(a1) was the superposed outer ring. In this case, the number of discretized terms of inner ring was only one less than that of the outer ring, i.e., $p = (q - 1)/3$, and the results are illustrated in Figure 1(c). There were only four pairs of terms of 0 and 2π in the superposed area. Simultaneously, there was merely one period increasing from 0 to 2π around each singularity anticlockwise. According to the definition of TC in Eq. (1), the TC of unit OVs in OVL is always –1. Thereafter, the phase shown in Figure 1(b1) was exchanged to be the superposed outer ring. Similarly, in this case, $p = (q + 1)/3$, and four positive unit OVs (TC = +1) were produced around where the phase that was clockwise increased from 0 to 2π [Figure 1(d)]. Generally, considering the different superposed OV beams, the only changes are in the numbers and signs of the unit OVs in OVL. Furthermore, the magnitude of TC of each OV remained unchanged, as obtained from previous references [21]. Consequently, an additional operation should be performed on the superposed phase to obtain HO-OVs from OVL.

To multiply TC of the unit OV in OVL, a multiplication factor, l, is applied to the superposed phase distribution as follows:

$$lm = \frac{1}{2\pi}\int_C \nabla\Big(l\psi(s)\Big)ds \tag{2}$$

and combined with Eq. (1), the phase, $\psi(s)$, of OVL can be substituted by $\psi_0(s)$ as follows:

$$\psi_0(s) = l\psi(s) \tag{3}$$

Thus, the phase term of OVL can be reconstructed as $\exp[j\psi_0(s)]$. Notably, the exponential function, e, is a periodic function, which truncates the phase into several periods, $0 - 2\pi$. Consequently, HO-TC of OV would be obtained in OVL. Figure 1 shows the schematic of the principle. Therein, TC of OV in OVL was multiplied by $l = 3$. The upper row is a 3D representation of the multiplication

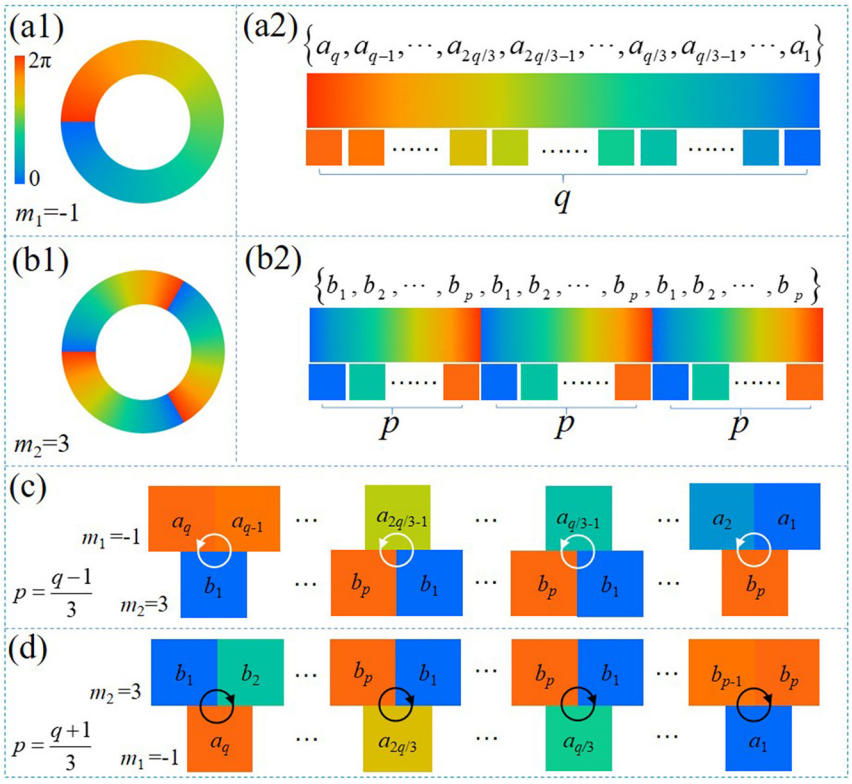

Figure 1: Schematic illustration of why TC of the unit OVs in OVL is always ±1. (a1) And (b1) OV beams with TCs of −1 and 3, respectively. (a2) And (b2) horizontal expansion and discrete arithmetic sequences. (c) And (d) superposition in two different cases, and the white and black circle arrows represent the negative and positive unit OVs, respectively.

process of one unit OV. The middle and lower rows represent the phase reconstruction of OVL and the magnification of the specific OV, respectively.

HO-OVL exhibits the modulation of the OV in a circular structure. However, to function as OAM during multiple microparticle manipulations, the HO-OVL mode should be arbitrarily modulated. To achieve this, the structures of the OV beams were shaped to desired modes by the holographic beam-shaping technique before the superposition [24]. The computer-generated hologram of the shaped OV is written as follows:

$$H_i(x,y) = \sum_{i=1}^{n} A_i \frac{1}{\int_0^T |c_2'(t)|dt} \int_0^T \varphi_i(x,y,t)|c_2'(t)|dt \quad (4)$$

where $H_i(x, y)$ represents a vortex beam along the arbitrary curves; A_i is a Gaussian function that regulates the amplitude distribution of the curve; n is a parameter that controls the width of the curve, the term $|c_2'(t)| = [x'_0(t)^2 + y'_0(t)^2]^{1/2}$ with $t \in [0, T = 2\pi]$; and $\varphi_i(x, y, t)$ is the phase term. The shaped OV beam is generated at the frequency plane:

$$G_i(\eta,\xi) = \int\int_{-\infty}^{\infty} H_i(x,y)\exp[-2j\pi(\eta x + \xi y)]dxdy \quad (5)$$

OVL is generated via the superposition of two shaped vortex beams and is written as follows:

$$G(\eta,\xi) = G_1(\eta,\xi) + G_2(\eta,\xi) \quad (6)$$

Equation (6) can be rewritten as a general formula for the complex amplitude of the light field:

$$G(\eta,\xi) = A(\eta,\xi)e^{j\psi(\eta,\xi)} \quad (7)$$

Applying l to the phase term of OVL, the complex amplitude, HO-OVL, can be reconstructed:

$$G_0(\eta,\xi) = A(\eta,\xi)e^{j\psi_0(\eta,\xi)} \quad (8)$$

In this case, the circular curve was selected as the major research object. Here, $x_0(t) = R_i \cos t$, $y_0(t) = R_i \sin t$, $n = 100$, $R_1 = 1.6$ mm, $R_2 = 1.9$ mm, $m_1 = 4$, $m_2 = -4$, and $N = |m_1 - m_2|$, where R_i is the parameter that controls the radius of the beam, n is the circular thickness, m_1 and m_2 are TCs of the two superposed OV beams, and N is the number of OVs on the ring. Figure 2(b1) shows the phase term of OVL. Assuming $l = 3$, the reshaped phase, ψ_0, and the final truncated phase are shown in Figure 2(b2) and (b3), respectively.

3 Generation and validation

To generate and verify the effectiveness of the proposed method, the experiment was set, as shown in Figure 3. The

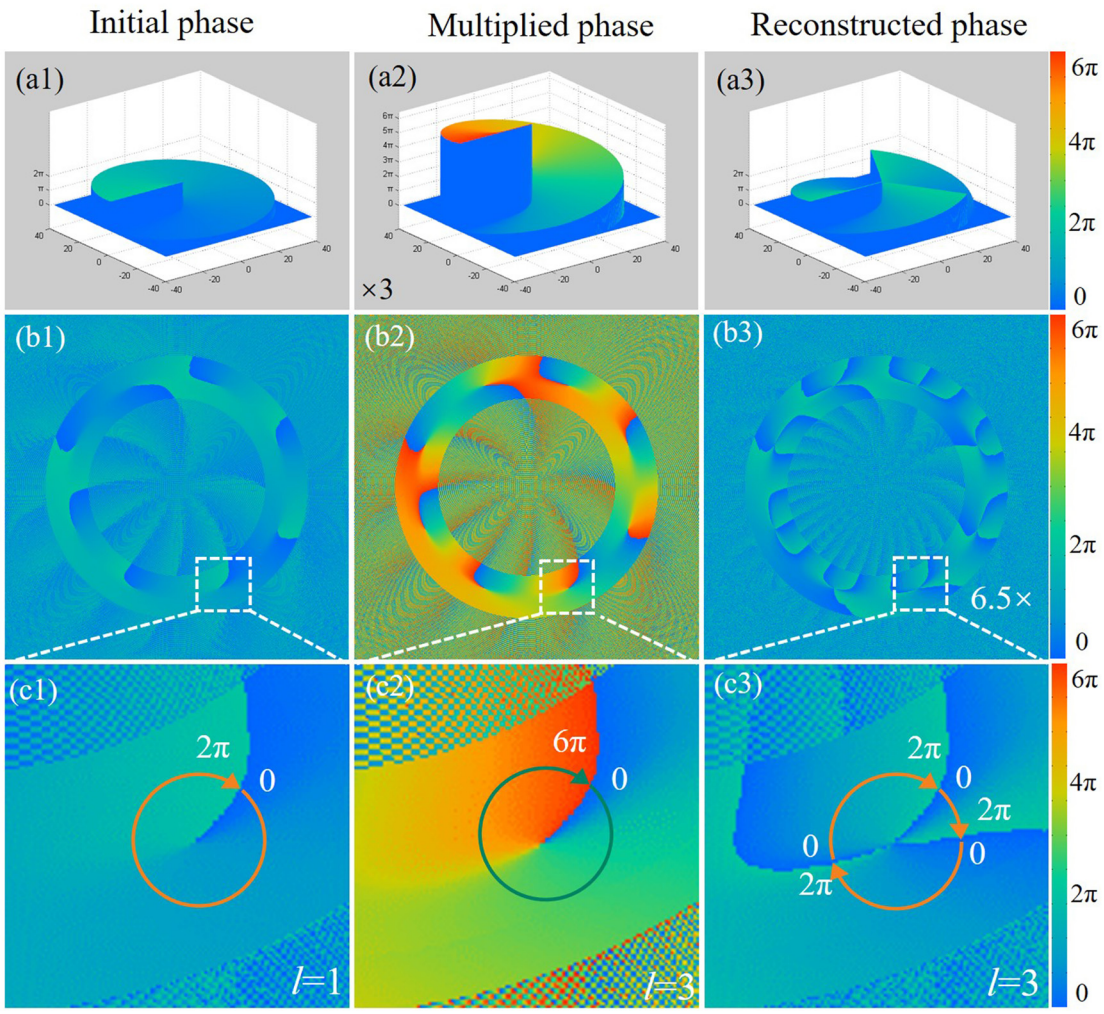

Figure 2: HO-TC generation via phase multiplication.
(a1)–(a3) Initial, multiplied, and HO phases of OV, respectively. (b1)–(b3) Phase reconstruction of OVL. (c1)–(c3) Magnification patterns of the specific OV phase.

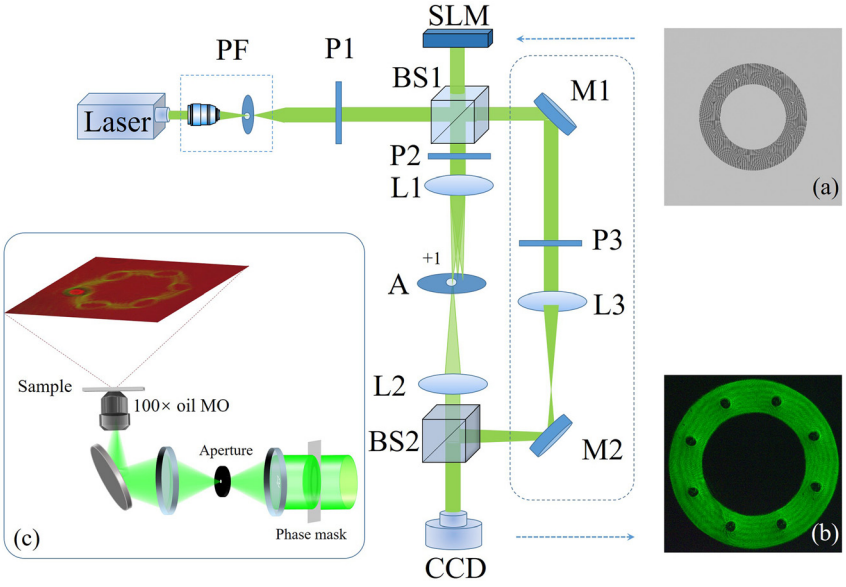

Figure 3: Schematic of the experimental setup. PF, pinhole filter; P1–P3, polarizers; BS1 and BS2, beam splitters; SLM, spatial light modulator; L1–L3, convex lenses; A, aperture; M1 and M2, mirrors; CCD, charge-coupled device.
(a) Amplitude-modulated phase mask, (b) intensity of HO-OVL recorded by CCD, and (c) module of the particle manipulation.

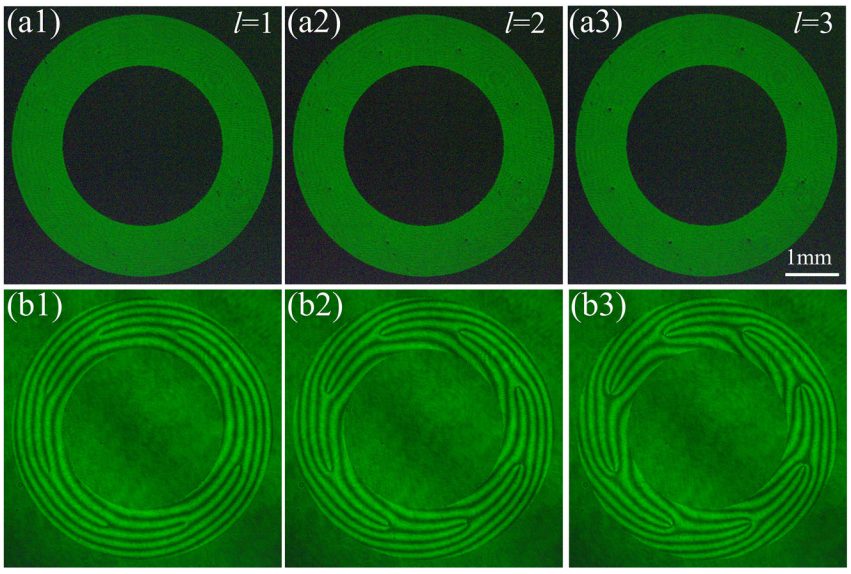

Figure 4: Interferograms of HO-OVL and a spherical beam.
(a1)–(a3) Experimental intensity patterns of l = 1, 2, and 3, respectively, and (b1)–(b3) their corresponding interferograms.

532-nm laser beam irradiated the spatial light modulator (SLM, HOLOEYE, PLUTO-VIS-016; pixel size, 8 × 8 μm^2; resolution, 1920 × 1080 pixels) after expanding and collimating. The beam was modulated by SLM and reflected onto a 4F system that is composed of two lenses (L1 and L2), with the same focal length (15 cm). Finally, it was recorded by a charge-coupled device (CCD, Basler acA1600-60gc; pixel size, 4.5 × 4.5 μm^2) on the second Fourier plane. The optical path that is encircled by the dotted lines is a reference light path to execute interference.

A binary mask (1024 × 1024 pixels) was designed to eliminate the stray light, as shown in Figure 3(a). It is expressed as $T = bw[A(r,\theta)] \times \exp\{i[l\varphi(r,\theta) + 2\pi x/d]\}$, where $bw(\cdot)$ is a binary function and d is the period of the blazed grating. Since OVL was produced on the SLM plane, the 4F system was employed to output and record HO-OVL at the desired position.

To verify the existence of OVs and determine their corresponding TCs in HO-OVL, a spherical beam was employed as reference light to execute interference. Figure 4 illustrates the intensity patterns and interferograms. The sizes of the dark cores increased with increasing l. A spiral fork fringe pattern appeared in the interferogram patterns at the corresponding position of each dark core. The results verified that OVs existed in HO-OVLs. Furthermore, TC of OV was determined by the fork number minus one, which is consistent with the default values of l. Consequently, HO-OVL was successfully generated in this case (Figure 5).

4 Results and discussion

To assign a significant role to OAM in HO-OVL, it was employed as a key parameter of l of each photon possessing OAM of $l\hbar$. The capacity of OAM of OV in the lattice was determined by the maximum of l. In this work, the multiplication times were up to 51 (i.e., l = 51), which is the maximum to the best of our knowledge. Moreover, the structure of the dark core gradually changed into a drop shape beyond that value (l = 51). However, HO-OVLs with increased OAM can be obtained for special applications if the phase mask and experimental elements are designed and arranged carefully, respectively.

To exploit OAM in HO-OVL, the distributions of OAM and the energy flow must be demonstrated and analyzed. The parameters of HO-OVL were changed to thicken the intensity ring for sufficient photons, where n = 150 and l = 1, 10, and 20, respectively. In experiments, OAM was difficultly determined in the solution. Consequently, OAM and the energy flow were numerically calculated by the previously reported methods [2, 36–38]. The equation of the energy flow is written as follows:

$$\boldsymbol{P}(\eta,\xi) = \frac{\epsilon_0}{4\omega}\mathrm{Im}[\boldsymbol{G}_0^*(\eta,\xi)\cdot(\nabla)\boldsymbol{G}_0(\eta,\xi)] \tag{9}$$

where ε_0 is the vacuum permittivity, $\omega = k\cdot c$ is the circular frequency of light, c is the velocity of light in a vacuum, and k is the wavenumber. OAM is typically deduced by the following equation [38]:

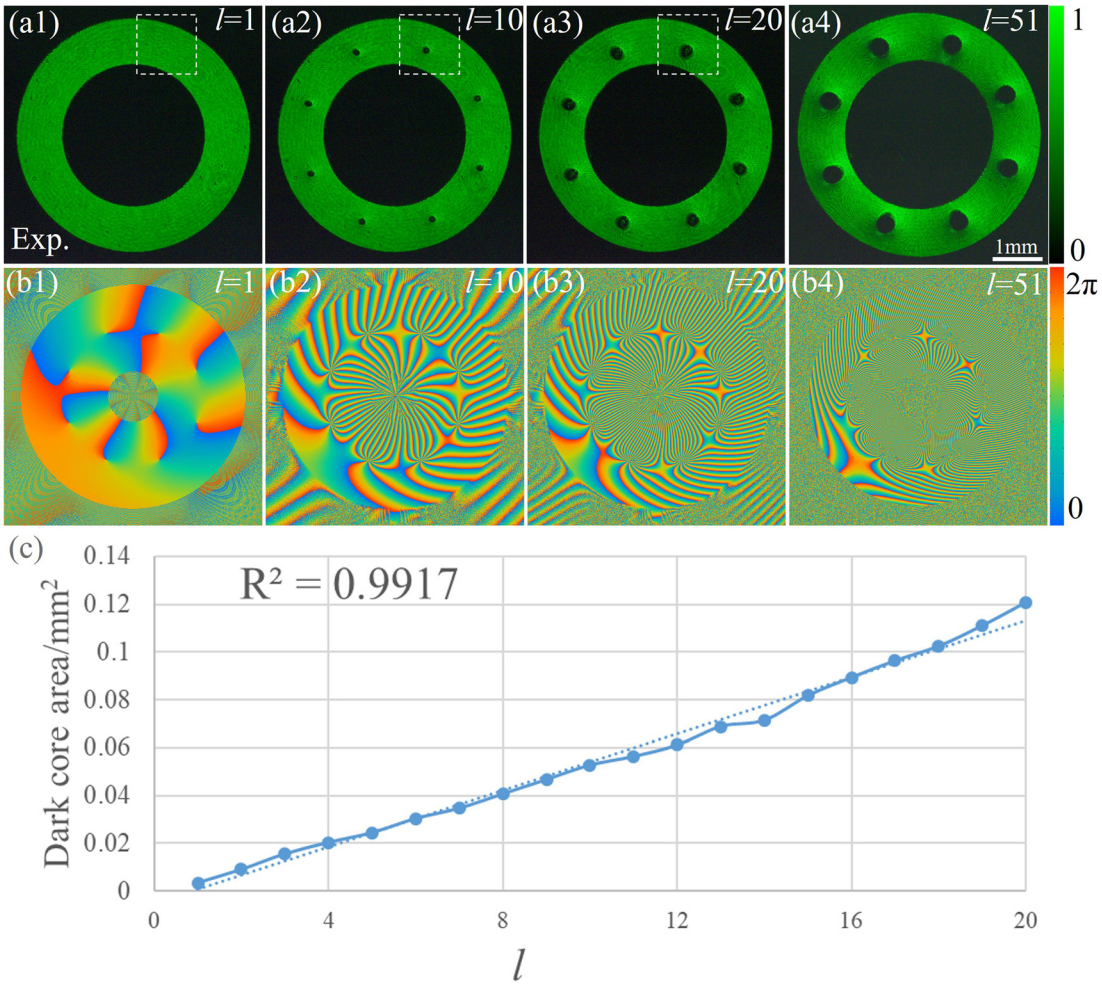

Figure 5: (a1)–(a4) HO-OVL intensity patterns with different ls (1, 10, 20, and 51, respectively). (b1)–(b4) Corresponding phase patterns of the top row. (c) Area of the dark core versus *l*.

$$\begin{aligned} \boldsymbol{J}(\eta,\xi) &= \frac{\epsilon_0}{2\omega}\boldsymbol{r}\times \mathrm{Im}[\boldsymbol{G}_0^*(\eta,\xi)\cdot(\nabla)\boldsymbol{G}_0(\eta,\xi)] \\ &= \eta\cdot P_\xi + \xi\cdot P_\eta \end{aligned} \tag{10}$$

where $\boldsymbol{r}$ is the position from the origin. Since the calculation center is the optical axis, the results cannot reflect the properties of OV on the ring. Therefore, the above equation requires a displacement to change the calculation center. Hence:

$$\boldsymbol{J}_0(\eta-\eta_0,\xi-\xi_0) = (\eta-\eta_0)\cdot P_{\xi-\xi_0} + (\xi-\xi_0)\cdot P_{\eta-\eta_0} \tag{11}$$

where η_0 and ξ_0 are the coordinate parameters that control the calculation center.

Employing the aforementioned theory, the simulations of the energy flow and OAM of HO-OVL were numerically performed with different *l*s. For comparison, the size of the dark core was designed to be constant with increasing *l*. Figure 6(a1)–(a3) shows the intensity patterns containing the energy flow. Therein, the white arrows represent the direction and magnitude of the flow. To observe the details, specific OVs were magnified, as displayed in Figure 6(b1)–(b3). It can be observed that the ring current of the energy flow was formed around each OV. Moreover, the ring current increased dramatically with increasing *l*. This trend also appeared in the density patterns of OAM [Figure 6(c1)–(c3)], which was calculated utilizing the center of the specific OV as the rotating axis of OAM.

To quantificationally analyze the change in the energy flow, OAM, and rotation speed with increasing *l*, the data at four sampling points marked in the second row were calculated and plotted [Figure 6(d1), (d2) and (d3)]. Among them, the rotation speed was numerically simulated via the method in Ref. [39] under our experimental conditions. The results indicated that the energy flow, OAM, and rotation speed increased monotonically with increasing *l*. Furthermore, the magnified times of the energy flow, OAM, and

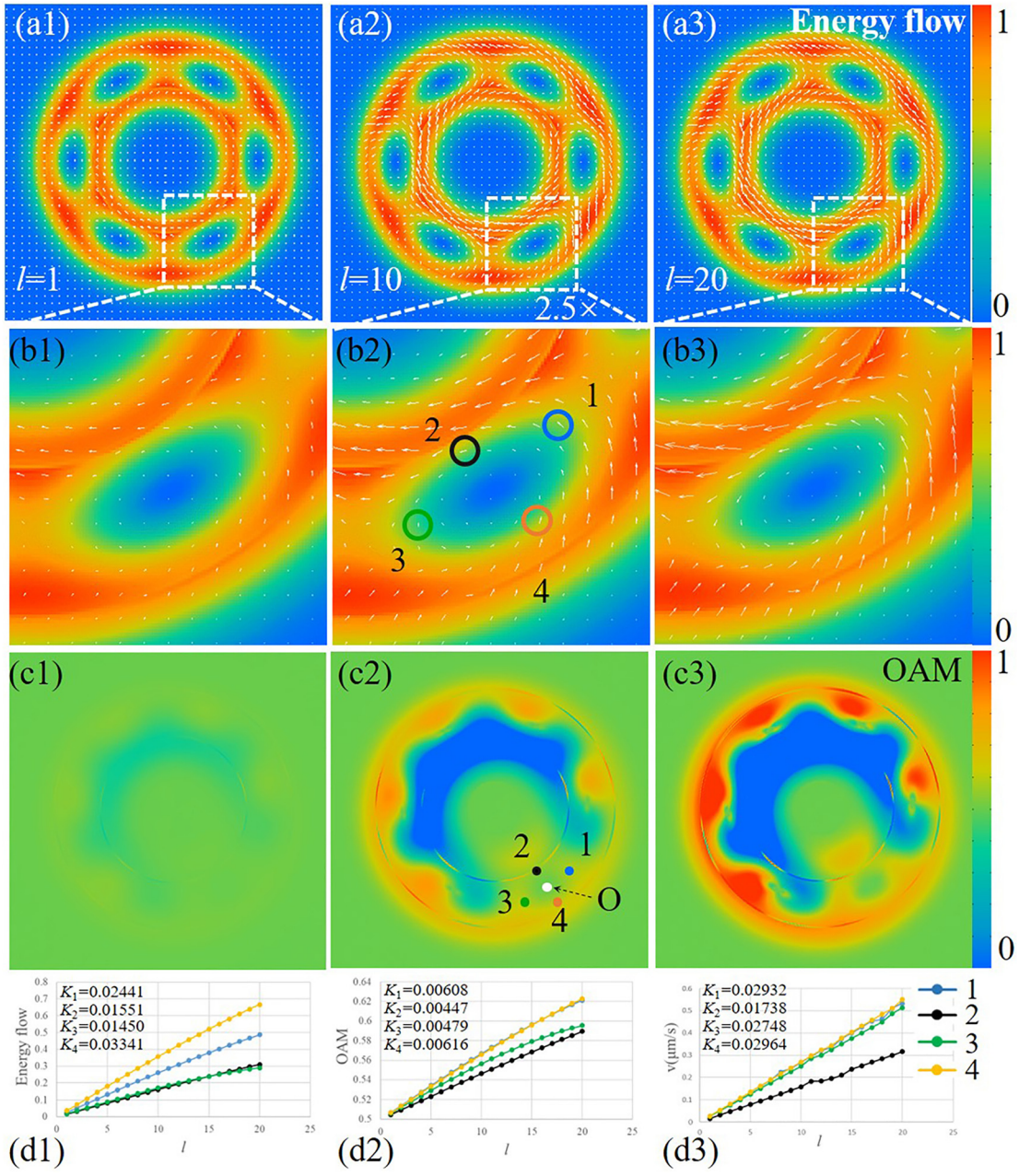

Figure 6: Change in the energy flow and OAM with increasing *l*.
(a1)–(a3) Energy flows, (b1)–(b3) local magnification of OVs in the lattice, and (c1)–(c3) OAM density distributions. The axis of symmetry is located at the center of the specific OV, i.e., at point O. (d1), (d2), and (d3) Energy flows, OAM, and rotation speed at specific points versus *l*, respectively. Note that energy flow and OAM are normalized, respectively.

rotation speed are approximately equal to the value of l. For instance, the times of the energy flow and OAM were both equal to 9.7 and 17.8 for l = 10 and 20 compared to l = 1, respectively. For a specific sampling point, the slopes of the fitting lines were different, whereas the times were approximately equivalent because of the different initial values. The results hinted that the unit OVs in HO-OVL could be employed to rotate and spin microparticles of different sizes.

To exploit OAM in OVL, i.e., assign it an essential role, microparticle manipulation experiments were conducted. Yeast cells were selected as the samples to highlight the applications in biosciences. Oil immersion microscope objective (1.2 NA, 100×) was employed to focus HO-OVL [Figure 3(c)] onto the samples.

We executed three groups of experiments to verify the capacity of OAM. Firstly, the yeast cell with a size of 5–8 μm

was irradiated by HO-OVL with $l = 1$ for 20 s. The cell was trapped in OV with slight Brownian motion. Subsequently, the beam was switched into HO-OVL with $l = 6$, and the cell began to spin under the influence of OAM. This process is shown in Figure 7(a1)–(a5) (details are contained in Visualization 1). In the experiments, the yeast cell stopped rotating after spinning at a certain angle (~90°). During the spinning of the cells, they always attained equilibrium, where OAM did not supply sufficient wrench force to continue the spin. This phenomenon is dominated by the shape match between the dark core and yeast cell. If the dark core occupying OV was a perfect circle, the cell would spin ceaselessly. The orientation location of the particles could be determined by shaping the structure of the dark core. Consequently, OAM of OV in the lattice would play a dominating role in rotating the cells. To the best of our knowledge, this is the first implementation of particle rotation by OVL.

Moreover, OAM could achieve complex motion comprising spin and revolution around OV (the second row demonstrates these properties). The yeast cell was alternatively irradiated by HO-OVL with $l = 10$. Here, the radius of OV was greater than that of the yeast, thus facilitating its capture by the ring around OV, followed by its rotation upon the application of OAM. Next, l was changed to 6, and the spinning of the yeast resumed, as shown in Figure 7(b1)–(b5) (refer to Visualization 2 for details). Compared with the single OV beam, one of the advantages of OVL is the fact that it contains multiple OVs. Consequently, HO-OVL can simultaneously manipulate multiple particles. This ability was demonstrated and verified by simultaneously rotating two yeast cells, as shown in Figure 7(c1)–(c5) (refer to Visualization 3 for details). More complex motions of the cell, as desired, could be obtained with more complex combinations of l.

Thus far, OAM has demonstrated tremendous ability in HO-OVL. To satisfy the special requirements of multiparticle manipulation, the versatile modes of HO-OVL should be freely controlled. Owing to the arbitrary curve technique, we generated HO-OVLs with specific modes, e.g., the triangular, heart-like, and hexagonal modes, as shown in Figure 8. TC of each OV in the lattice was multiplied into 10. Despite employing the same mode, the curve function was not unique. Owing to the difference in the curve function, different curve parameters were adjusted based on the experiment. Figure 8 shows the intensities and corresponding phase distributions of the three modes. For the triangular HO-OVL, the equations and parameters were set as $x_0(t) = R_i(-2\cos t + 0.54\cos 2t)$, $y_0(t) = R_i(-2\cos t - 0.54\cos 2t)$,

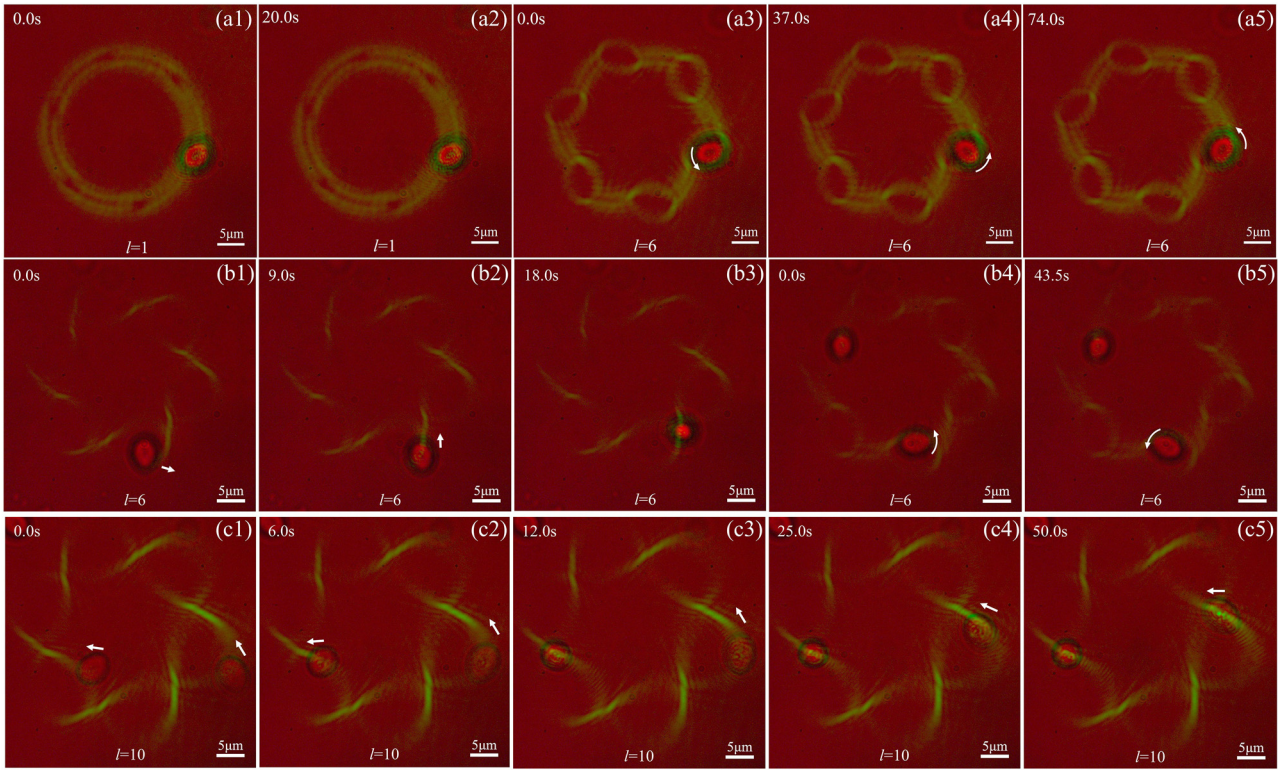

Figure 7: Manipulation of yeast cells by HO-OVL.
(a1)–(a5) Irradiation of the yeast cell by HO-OVL with $l = 1$, which was subsequently switched to $l = 6$. (b1)–(b5) Irradiation of the yeast cell by HO-OVL with $l = 10$, which was switched into $l = 6$. (c1)–(c5) Simultaneous rotations of two yeast cells.

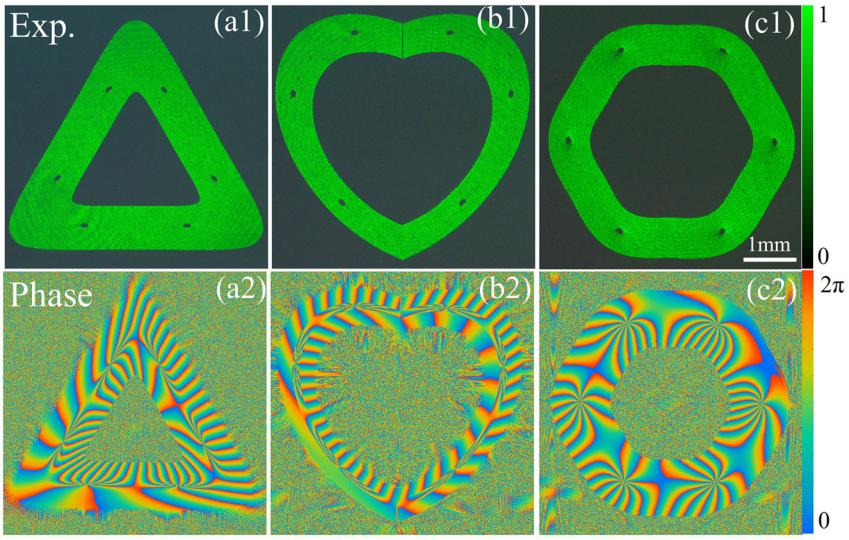

Figure 8: HO-OVL with versatile modes. (a1)–(c1) Intensity patterns of triangular, heart-like, and hexagonal HO-OVLs. (a2)–(c2) Corresponding phase distributions of (a1)–(c1). $l = 10$ in all the instances.

$n = 100$, $R_1 = 0.8$ mm, $R_2 = 1.1$ mm, $m_1 = 3$, and $m_2 = -3$. For the heart-like HO-OVL, the equations and parameters were set as $x_0(t) = |R_i(3\cos t - 2\cos 2t)|$, $y_0(t) = -R_i(2\cos t - 3\cos t)$, $n = 100$, $R_1 = 0.8$ mm, $R_2 = 0.9$ mm, $m_1 = 3$, and $m_2 = -3$. For the hexagonal HO-OVL, the equations and parameters were set as $x_0(t) = R_i\cos t(1 - 0.035\cos 6t)$, $y_0(t) = R_i\cos t(1 - 0.035\cos 6t)$, $n = 100$, $R_1 = 1.6$ mm, $R_2 = 1.9$ mm, $m_1 = 3$, and $m_2 = -3$. Employing an arbitrary curve function, the corresponding HO-OVL could be explicitly produced, as desired.

Comparing with the holographic optical tweezers [40, 41], the proposed optical tweezers based on HO-OVL can trap multiple particles, and simultaneously execute complex motion, especially the spin and orbital rotations. The dark cores and OAM of the proposed HO-OVL were pivotal, and this would facilitate new potential applications that can be limited only by our imagination. From the experiments, the yeast cells did not rotate a complete period due to the asymmetry of the dark cores. We believe that the rotation with a complete period, even the orbital rotation on the whole OVL, can be realized by accurately modifying the size, structure, and intensity distribution of the unit OVs. The issue will be studied in the near future. Further, the force field distribution and more complex motions of multiple particles, especially the nanoparticles, are the other areas that should be extensively studied soon.

5 Conclusions

Summarily, we proposed HO-OVL with controllable modes employing the phase multiplication and arbitrary curving techniques. To guarantee beam quality, the OAM order of each OV in the lattice was increased up to 51, exceeding the limit of the traditional OVL. Thus, OAM of each OV in HO-OVL was exploited and unleashed. The manipulation of the yeast cell indicated that HO-OVL could induce the complex motion of particles under the influence of OAM. Our results can pave the way for future trapping and manipulation of multiple microparticles, particularly in biosciences [29–32].

Author contributions: All the authors have accepted responsibility for the entire content of this submitted manuscript and approved submission.
Research funding: National Natural Science Foundation of China (Nos. 11974102, 11704098, 11974101), State Key Laboratory of Transient Optics and Photonics (No. SKLST201901), and Key Scientific Research Projects of Institutions of Higher Learning of Henan Province Education Department (No. 21zx002).
Conflict of interest statement: The authors declare no competing financial interest.

References

[1] J. F. Nye and M. V. Berry, "Dislocations in wave trains," *Proc. R. Soc. Lond.*, vol. A336, pp. p165–p190, 1974.
[2] L. Allen, M. W. Beijersbergen, R. Spreeuw, and J. Woerdman, "Orbital angular momentum of light and the transformation of Laguerre–Gaussian laser modes," *Phys. Rev. A*, vol. 45, p. 8185, 1992.
[3] X. Qiu, F. Li, W. Zhang, Z. Zhu, and L. Chen, "Spiral phase contrast imaging in nonlinear optics: seeing phase objects using invisible illumination," *Optica*, vol. 5, p. 208, 2018.
[4] X. Z. Li, H. X. Ma, H. Zhang, et al., "Is it possible to enlarge the trapping range of optical tweezers via a single beam?" *Appl. Phys. Lett.*, vol. 114, p. 081903, 2019.

[5] X. Z. Li, H. Zhang, H. X. Ma, et al., "Grafted optical vortex with controllable orbital angular momentum distribution," *Opt. Express*, vol. 27, p. 22930, 2019.
[6] T. Chantakit, C. Schlickriede, B. Sain et al., "All-dielectric silicon metalens for two-dimensional particle manipulation in optical tweezers," *Photonics Res.*, vol. 8, p. 1435, 2020.
[7] J. A. Rodrigo, M. Angulo, and T. Alieva, "All-optical motion control of metal nanoparticles powered by propulsion forces tailored in 3D trajectories," *Photonics Res.*, vol. 9, no. 1, 2021, https://doi.org/10.1364/prj.408680.
[8] J. Wang, J.-Y. Yang, I. M. Fazal, et al., "Terabit free-space data transmission employing orbital angular momentum multiplexing," *Nat. Photonics*, vol. 6, p. 488, 2012.
[9] M.-J. Liu, J. Chen, Y. Zhang, Y. Shi, C.-L. Zhao, and S.-Z. Jin, "Generation of coherence vortex by modulating the correlation structure of random lights," *Photonics Res.*, vol. 7, p. 1485, 2019.
[10] F. Wen, X. Zhang, H. Ye, et al., "Efficient and tunable photoinduced honeycomb lattice in an atomic ensemble," *Laser Photonics Rev.*, vol. 12, p. 1800050, 2018.
[11] Y. Dai, Z. Zhou, A. Ghosh, et al., "Plasmonic topological quasiparticle on the nanometre and femtosecond scales," *Nature*, vol. 588, p. 616, 2020.
[12] T. Cookson, K. Kalinin, H. Sigurdsson, et al., "Geometric frustration in polygons of polariton condensates creating vortices of varying topological charge," *Nat. Commun.*, vol. 12, p. 2120, 2018.
[13] S. Albaladejo, M. I. Marqués, F. Scheffold, and J. J. Sáenz, "Giant enhanced diffusion of gold nanoparticles in optical vortex fields," *Nano Lett.*, vol. 9, p. 3527, 2009.
[14] S. Tsesses, E. Ostrovsky, K. Cohen, B. Gjonaj, N. H. Lindner, and G. Bartal, "Optical skyrmion lattice in evanescent electromagnetic fields," *Science*, vol. 361, p. 993, 2018.
[15] Y. Qian, Y. Shi, W. Jin, F. Hu, and Z. Ren, "Annular arrayed-Airy beams carrying vortex arrays," *Opt. Express*, vol. 27, p. 18085, 2019.
[16] Y. K. Wang, H. X. Ma, L. H. Zhu, Y. P. Tai, and X. Z. Li, "Orientation-selective elliptic optical vortex array," *Appl. Phys. Lett.*, vol. 116, p. 011101, 2020.
[17] X. Qiu, F. Li, H. Liu, X. Chen, and L. Chen, "Optical vortex copier and regenerator in the Fourier domain," *Photonics Res.*, vol. 6, p. 641, 2018.
[18] S. Fu, T. Wang, and C. Gao, "Perfect optical vortex array with controllable diffraction order and topological charge," *J. Opt. Soc. Am. A*, vol. 33, p. 1836, 2016.
[19] C.-S. Guo, Y.-N. Yu, and Z. Hong, "Optical sorting using an array of optical vortices with fractional topological charge," *Opt. Commun.*, vol. 283, p. 1889, 2010.
[20] S. Franke-Arnold, J. Leach, M. J. Padgett, et al., "Optical ferris wheel for ultracold atoms," *Opt. Express*, vol. 15, p. 8619, 2007.
[21] X. He, P. Xu, J. Wang, and M. J. O. E. Zhan, "Rotating single atoms in a ring lattice generated by a spatial light modulator," *Opt. Express*, vol. 17, p. 21007, 2009.
[22] A. V. Ponomarev, S. Denisov, and P. Hänggi, "AC-driven atomic quantum motor," *Phys. Rev. Lett.*, vol. 102, p. 230601, 2009.
[23] H. Ma, X. Li, Y. Tai, et al., "Generation of circular optical vortex array," *Ann. Phys. Berlin*, vol. 529, p. 1700285, 2017.
[24] L. Li, C. Chang, X. Yuan, et al., "Generation of optical vortex array along arbitrary curvilinear arrangement," *Opt. Express*, vol. 26, p. 9798, 2018.
[25] B. Chen, J. Geng, F. Zhou, L. Song, H. Shen, and N. Xu, "Quantum state tomography of a single electron spin in diamond with Wigner function reconstruction," *Appl. Phys. Lett.*, vol. 114, p. 041102, 2019.
[26] X. Li and H. Zhang, "Anomalous ring-connected optical vortex array," *Opt. Express*, vol. 28, p. 13775, 2020.
[27] Y. Liu, G. Bartal, X. Zhang, M. Liu, and T. Zentgraf, "Light-driven nanoscale plasmonic motors," *Nat. Nanotechnol.*, vol. 5, pp. 570–573, 2010.
[28] T. Wu, T. A. Nieminen, S. Mohanty, et al., "A photon-driven micromotor can direct nerve fibre growth," *Nat. Photonics*, vol. 6, p. 62, 2012.
[29] C. Deufel, S. Forth, C. R. Simmons, S. Dejgosha, and M. D. Wang, "Nanofabricated quartz cylinders for angular trapping: DNA supercoiling torque detection," *Nat. Methods*, vol. 4, p. 223, 2007.
[30] M. Reichert and H. Stark, "Circling particles and drafting in optical vortices," *J Phys. Condens. Mater.*, vol. 16, p. S4085, 2004.
[31] V. Garcés-Chávez, D. McGloin, H. Melville, W. Sibbett, and K. Dholakia, "Simultaneous micromanipulation in multiple planes using a self-reconstructing light beam," *Nature*, vol. 419, p. 145, 2002.
[32] A. E. Carruthers, J. S. Walker, A. Casey, A. J. Orr-Ewing, and J. P. Reid, "Selection and characterization of aerosol particle size using a bessel beam optical trap for single particle analysis," *Phys. Chem. Chem. Phys.*, vol. 14, p. 6741, 2012.
[33] L. Chen, W. Zhang, Q. Lu, and X. Lin, "Making and identifying optical superpositions of high orbital angular momenta," *Phys. Rev. A*, vol. 88, p. 053831, 2013.
[34] W. Zhang, and L. Chen, "High-harmonic-generation-inspired preparation of optical vortex arrays with arbitrary-order topological charges," *Chin. Opt. Lett.*, vol. 16, p. 030501, 2018.
[35] J. F. Nye, M. V. Berry, and F. C. Frank, "Dislocations in wave trains," *Proc. R. Soc. A Math. Phys.*, vol. 336, p. 165, 1974.
[36] A. T. O'Neil, I. MacVicar, L. Allen, and M. J. Padgett, "Intrinsic and extrinsic nature of the orbital angular momentum of a light beam," *Phys. Rev. Lett.*, vol. 88, p. 053601, 2002.
[37] A. Canaguier-Durand, A. Cuche, C. Genet, and T. W. Ebbesen, "Force and torque on an electric dipole by spinning light fields," *Phys. Rev. A*, vol. 88, p. 033831, 2013.
[38] D. B. Ruffner and D. G. Grier, "Optical forces and torques in nonuniform beams of light," *Phys. Rev. Lett.*, vol. 108, p. 173602, 2012.
[39] Y. Roichman, B. Sun, Y. Roichman, J. Amato-Grill, and D. G. Grier, "Optical forces arising from phase gradients," *Phys. Rev. Lett.*, vol. 100, p. 013602, 2008.
[40] Y. Cai, S. Yan, Z. Wang, et al., "Rapid tilted-plane Gerchberg–Saxton algorithm for holographic optical tweezers," *Opt. Express*, vol. 28, p. 12729, 2020.
[41] Y. Liang, S. Yan, Z. Wang, et al., "Simultaneous optical trapping and imaging in the axial plane: a review of current progress," *Rep. Prog. Phys.*, vol. 83, p. 032401, 2020.